Retrieval and Prediction of Three-Dimensional Displacements by Combining the DInSAR and Probability Integral Method in a Mining Area

Chuanguang Zhu [ID], Zhengshuai Wang, Peixian Li, Mahdi Motagh [ID], Liya Zhang, Zongli Jiang, and Sichun Long

Abstract—Monitoring ground displacement produced by underground mining is essential to ensure the safety of infrastructure over mining areas. Differential synthetic aperture radar (DInSAR) can only obtain the 1-D [i.e., along the line-of-sight (LOS) direction] displacement component. In this study, we present an improved algorithm for retrieving and predicting 3-D displacement fields induced by underground mining based on the LOS displacement derived from DInSAR and the probability integral method (PIM). Whole parameters included in the standard PIM model are involved in the improved algorithm. In addition, the interaction between multiple working panels is considered and incorporated into the model. Next, a stochastic optimization technique hybridizing the cultural algorithm and random particle swarm optimization has been designed to retrieve model parameters, which can be used to retrieve and predict the 3-D displacement field. Simulated experiments show that the root mean square errors (RMSEs) are 10, 12, and 17 mm in the vertical, east-west, and north-south directions, respectively, by comparing the simulated and retrieved 3-D displacement. Furthermore, the capability of the proposed method is investigated and validated in the Xuehu mining area of China using three ALOS PALSAR acquisitions. Our results agree well with leveling measurements in the vertical direction with an RMSE of 38 mm. Although the retrieved horizontal displacement cannot be validated due to a lack of field surveys, these displacement fields coincide spatially with the evolution of mining excavation.

Index Terms—Cultural algorithm and random particle swarm optimization (CA-rPSO), mining displacement, probability integral method (PIM), three-dimensional (3-D) displacement.

Chuanguang Zhu, Liya Zhang, Zongli Jiang, and Sichun Long are with the Key Laboratory of Coal Resources Clean-Utilization & Mine Environment Protection of Hunan Province, Hunan University of Science & Technology, Xiangtan 411201, China (e-mail: zhucg@hnust.edu.cn; lyzhang47@163.com; jiangzongli@hnust.edu.cn; sclong@hnust.edu.cn).

Zhengshuai Wang is with the School of Geography, Geodesy and Planning, Jiangsu Normal University, Xuzhou 221116, China (e-mail: wzs1001@163.com).

Peixian Li is with the College of Geoscience and Surveying Engineering, China University of Mining & Technology (Beijing), Beijing 100083, China (e-mail: pxlicumt@126.com).

Mahdi Motagh is with the Section of Remote Sensing and Geoinformatics at GFZ German Research Centre for Geosciences, Potsdam, Germany and also with the Institute of Photogrammetry and Geoinformation, Leibniz University Hannover (LUH), 30167 Hannover, Germany (e-mail: motagh@gfz-potsdam.de).

Digital Object Identifier 10.1109/JSTARS.2020.2978288

I. INTRODUCTION

MINING-INDUCED displacement fields generally have a spatial extent of hundreds of meters [1]. This displacement can cause many serious environmental hazards, such as the collapse of roads, bridges, buildings, and other infrastructure located in the subsidence trough [2]–[4]. Therefore, early monitoring and measurement of these displacements is imperative to better understand the hazards and help the government or enterprise assess potential damage and make better decisions to minimize the impact [3].

Conventionally, mining-induced displacement have been measured using field-survey methods such as precise leveling, total stations and global positioning system based on a few sparse points [5], [6]. However, these field-survey methods are labor intensive and time consuming. Moreover, it is rather difficult to attain a reasonable damage assessment of buildings based on these sparse points [4]–[7].

Over the last two decades, differential synthetic aperture radar (DInSAR) has been proven to be a powerful technique for producing measurements of displacement caused by earthquakes [8], [9], landslides [10], groundwater overexploitation [11], and extraction of underground mining [12] with high precision (centimeter to millimeter) and high spatial resolution over large areas. However, only 1-D displacement along the line-of-sight (LOS) direction from the satellite to the ground can be detected using the DInSAR technique, as the SAR images are acquired in side-looking mode. In particular, the geometry of the displacement induced by underground mining is complicated compared with that induced by other human activities [13]. Generally, there are large horizontal displacement components that cannot be ignored. 3-D ground displacements are essential to assess mining-induced damage to infrastructure.

Over the past few years, several approaches have attempted to retrieve 3-D ground displacements. For instance, Ng *et al.* [14] retrieved 3-D displacements induced by underground mining using multiple interferometric pairs from ascending and descending orbits that have different LOS directions. He *et al.* [15] obtained 2-D (vertical and flight directions) time-series displacements due to open-pit mining from 11 ALOS PALSAR observations by coupling DInSAR with multiple-aperture InSAR (MAI) techniques over an open-pit mining area. However, these methods still have significant limitations. For example, a necessary prerequisite to success of the method adopted in

[14] is that at least three interferometric pairs with significantly different incidence angles are available, which is usually very difficult to achieve due to a finite number of SAR satellites. In addition, the accuracy of the displacement retrieved along the north-south direction is not high because of the polar orbits currently adopted by SAR satellites. Moreover, spatial resolution has been sacrificed by the MAI technique in order to obtain the displacement in the azimuth direction [16], [17]. The MAI technique is highly sensitive to the quality of coherence, which is mainly affected by temporal and geometrical baselines and atmospheric artifacts, particularly in mining areas with dense vegetation [18].

For mining-induced displacement fields, there exists a ratio between the horizontal displacement and the gradient of vertical displacement [19]. This ratio (also referred as the horizontal displacement constant) can generally be considered constant in the same mining area. Exploiting this characteristic and assuming the ratio as known, a new method was proposed to retrieve 3-D displacement using only one interferometric pair [20]. Obviously, considering the ratio to be a constant and known parameter is a gross oversimplification of the theoretical mechanism of mining-induced deformation [2]. In addition, some pixels with no displacement must be accurately selected in advance with this method, which is challenging due to the irregular subsidence trough caused by irregular work panels and complicated geologic conditions in mining areas. Thus, the application of this method is somewhat limited in practice.

Recently, a new approach (referred to as InSAR-PIM) for estimating 3-D mining-induced displacement has been presented in [2], in which the relationship between the model parameters of the probability integral method (PIM) and the InSAR-derived deformation along the LOS direction was first established. Next, a genetic algorithm was used to estimate these parameters, by which 3-D displacement can be predicted using the PIM [2], [18], [21]. However, this method has also simplified the PIM to a certain extent, i.e., not all parameters of the PIM are involved. In fact, each parameter in the PIM is different due to the inclination of coal seams, which is also affected by other working or abandoned panels, and has a specific contribution to ground displacement. In addition, only one working panel was considered in [2], [18], and [21].

In this article, we propose an improved algorithm for retrieving all model parameters of the PIM using LOS deformation derived from interferometric pairs with the same viewing geometry. First, all parameters are involved to retrieve and predict the 3-D displacement fields considering the complex underground mining conditions.

Furthermore, the superimposition of displacements and the influence on the estimation of PIM parameters due to the interaction of multiple working panels are considered and incorporated in the improved algorithm. To ensure the reliability and accuracy of the estimation of parameters, a method hybridizing the cultural algorithm and random particle swarm optimization (CA-rPSO) model is presented to solve the optimization problem in high-dimensional space. Finally, this method can facilitate the assessment of possible damage to structures attributed to the truly full model-based parameter inversion.
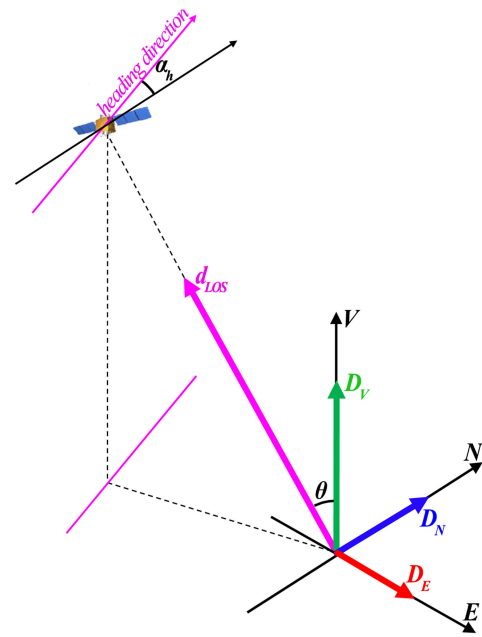

Fig. 1.   Decomposition of LOS deformation in 3-D (modified from [14], [23]).

II. METHODOLOGY

A. Overview of the InSAR-PIM Method

Generally, the ground deforms in the horizontal and vertical directions due to underground mining. Thus, the InSAR-derived deformation along the LOS (d_{LOS}) direction is a composite of the vertical, east-west, and north-south displacement components (see Fig. 1), which can be expressed as follows [22], [23]:

$$d_{\mathrm{LOS}} = [\cos\theta \;\; -\sin\theta\cos\alpha_h \;\; \sin\theta\sin\alpha_h] \begin{bmatrix} D_V \\ D_E \\ D_N \end{bmatrix} \quad (1)$$

where θ denotes the incidence angle of the SAR sensor at the measurement point, α_h denotes the azimuth of the satellite's flight direction (positive clockwise from North) and, D_V, D_E, and D_N are the displacement in the vertical, east-west, and north-south directions, respectively [23].

The ratio of maximal horizontal displacement to maximal vertical displacement is generally in the range of 0.1–0.4 [19], [24]. This means that horizontal displacement can reach 360–1200 mm when the maximum vertical displacement reaches 3000 mm. Therefore, horizontal displacement cannot be ignored. A very smart approach, i.e., InSAR-PIM, which couples the InSAR-derived deformation and the PIM, has been presented to retrieve 3-D mining-induced displacement fields using only one interferometric pair [2].

The PIM, developed from probability density function and random medium theory, is the most popular method used for predicting 3-D displacement due to underground mining [25]–[27]. According to the PIM, after extraction of one working panel, the displacement in the vertical $D_V(x, y)$, east-west $D_E(x, y)$, and north-south $D_N(x, y)$ directions at a ground point (x, y) can

be expressed as follows [18], [19]:

$$\begin{cases} D_V\left(x,\ y\right) = \frac{1}{W_0}W^\circ\left(x\right)\cdot W^\circ\left(y\right) \\ D_E\left(x,\ y\right) = \frac{1}{W_0}\left[U^\circ\left(x\right)\cdot W^\circ\left(y\right)\cdot\cos\phi_E\right. \\ \qquad\qquad\left. +U^\circ\left(y\right)\cdot W^\circ\left(x\right)\cdot\sin\phi_E\right] \\ D_N\left(x,\ y\right) = \frac{1}{W_0}\left[U^\circ\left(x\right)\cdot W^\circ\left(y\right)\cdot\cos\phi_N\right. \\ \qquad\qquad\left. +U^\circ\left(y\right)\cdot W^\circ\left(x\right)\cdot\sin\phi_N\right] \end{cases} \quad (2)$$

with

$$W_0 = m\cdot q\cdot\cos\alpha \quad (3)$$

$$\begin{cases} W^\circ\left(x\right) = W\left(x,\ r\right) - W\left(x-l,\ r\right) \\ W^\circ\left(y\right) = W\left(y,\ r_1\right) - W\left(y-L,\ r_2\right) \\ W\left(x,\ r\right) = \frac{W_0}{2}\left[erf\left(\sqrt{\pi}\frac{x}{r}\right)\right] + 1 \end{cases} \quad (4)$$

$$\begin{cases} U^\circ\left(x\right) = U\left(x,\ r\right) - U\left(x-l,\ r\right) \\ U^\circ\left(y\right) = U\left(y,\ r_1\right) - U\left(y-L,\ r_2\right) \\ \qquad +W\left(y,\ r_1\right)\cdot\cot\theta_0 - W\left(y-L,\ r_2\right)\cdot\cot\theta_0 \\ U\left(x,\ r\right) = b\cdot W_0\cdot\exp\left(-\pi\frac{x^2}{r^2}\right) \end{cases} \quad (5)$$

In (2)–(5), the following can be observed.

1) W_0 and q are the maximum subsidence and subsidence factor under critical/supercritical extraction of a working panel with thickness of m and dip angle of α, respectively.

2) $W^\circ(x)$ and $W^\circ(y)$ denote the vertical displacements under finite extraction along the strike and dip profiles, where $W(x,\ r)$, $W(x-1,\ r)$, $W(y,\ r_1)$, and $W(y-L,\ r_2)$ represent the vertical displacements under semi-infinite extraction along the strike and dip profiles, respectively.

3) $U^\circ(x)$ and $U^\circ(y)$ denote the horizontal displacements under finite extraction along the strike and dip profiles, respectively.

4) $erf(\sqrt{\pi}\frac{x}{r}) = \frac{2}{\sqrt{\pi}}\int_0^{\sqrt{\pi}\frac{x}{r}}\exp(-u^2)du$, which represents the probability density function.

5) $l = D_3 - s_3 - s_4$ and $L = (D_1 - s_1 - s_2)\frac{\sin(\theta_0+\alpha)}{\sin(\theta_0)}$ represent the effective lengths to calculate along the strike and dip directions. θ_0 is the mining propagation angle. s_3, s_4, s_1, and s_2 (illustrated in Fig. 2) are the offsets of inflection points along the left-strike, right-strike, down-dip, and up-dip directions, respectively.

6) r, r_1, and r_2 are related to the formation of $r = \frac{H}{\tan\beta}$, $r_1 = \frac{H_1}{\tan\beta_1}$, and $r_2 = \frac{H_2}{\tan\beta_2}$, where r, H, and β denote the radii of major influence, the mining depth, and the angle of major influence along the strike profile, while $[r_1,\ H_1,\ \beta_1]$ and $[r_2,\ H_2,\ \beta_2]$ represent the down-dip and up-dip profiles, respectively. Generally, $\beta = \beta_1 = \beta_2$.

7) φ_E and φ_N denote the angles between the advancing direction and the east-west and north-south directions measured counter clockwise (illustrated in Fig. 2) from the advancing direction.

8) b is the horizontal displacement factor, which is the ratio of the maximum horizontal displacement to the maximum vertical displacement.
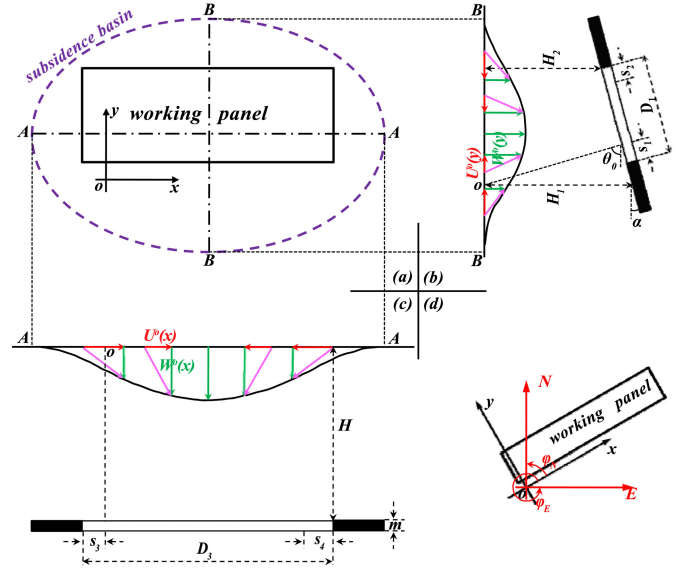

Fig. 2. (a) Subsidence basin caused by the extraction of a working panel. (b) After extraction of the working panel, the ground movements (pink line) along profile of the major section in the dip direction (i.e., B-B), which is composed of horizontal (red line) and vertical (green) movements. (c) Ground movements in the strike direction (i.e., A-A). (d) Geometric parameters of the working panel in the Geodetic coordinate system. (modified from [19]).

Generally, these geometric parameters, i.e., $P_G = [m,\ \alpha,\ H,\ H_1,\ H_2,\ D_1,\ D_3,\ \phi_E,\ \phi_N]$ can be obtained from designed maps, which are known. These model parameters of the PIM $P_M = [q,\ \theta_0,\ \tan\beta,\ s_1,\ s_2,\ s_3,\ s_4,\ b]$ need to be determined in advance in order to predict 3-D displacements. Yang *et al.* [2] assumed for simplicity that s_3 and s_4 are equal, which may not be in line with reality. Therefore, we consider all model parameters in P_M as independent in our method. The influence when s_3 and s_4 are unequal to the estimation of P_M will be discussed in Section III in detail. Then, (2) can be rewritten for simplicity as follows:

$$\begin{cases} D_V\left(x,\ y\right) = f_1\left(x,\ y,\ P_G,\ P_M\right) \\ D_E\left(x,\ y\right) = f_2\left(x,\ y,\ \phi_E,\ P_G,\ P_M\right) \\ D_N\left(x,\ y\right) = f_2\left(x,\ y,\ \phi_N,\ P_G,\ P_M\right) \end{cases} \quad (6)$$

If there are multiple working panels (e.g., K), the cumulative 3-D displacement at ground point $(x,\ y)$ can be expressed as follows:

$$\begin{cases} D_V\left(x,\ y\right) = \sum_{i=1}^{K} D_{V,\ i}\left(x,\ y\right) = \sum_{i=1}^{K} f_1\left(x,\ y,\ P_{G,\ i},\ P_{M,\ i}\right) \\ D_E\left(x,\ y\right) = \sum_{i=1}^{K} D_{E,\ i}\left(x,\ y\right) \\ \qquad = \sum_{i=1}^{K} f_2\left(x,\ y,\ \phi_E,\ P_{G,\ i},\ P_{M,\ i}\right) \\ D_N\left(x,\ y\right) = \sum_{i=1}^{K} D_{N,\ i}\left(x,\ y\right) \\ \qquad = \sum_{i=1}^{K} f_2\left(x,\ y,\ \phi_E,\ P_{G,\ i},\ P_{M,\ i}\right) \end{cases} \quad (7)$$

The unknown PIM parameter $P_{M,i}$ is related to rock properties and geometric parameter $P_{G,i}$. Generally, $P_{G,i}$ can be assumed to be the same when all working panels are located in the same coal seam. As normally many InSAR measurements (or pixels) are available over mining areas, it is possible to estimate P_M and alleviate the influence of noise and even gross errors contained in the InSAR measurements by the least-squares method.

B. Estimating PIM Parameters Using CA-rPSO

Mathematically, P_M can be estimated by minimizing the L2 norm of σ

$$\sigma = \mathrm{LOS}_o\left(\mathbf{X}\right) - \mathrm{LOS}_p\left(\mathbf{X},\ P_G,\ P_M\right) \tag{8a}$$

$$\|\sigma\|_2 = \min \tag{8b}$$

where $\mathrm{LOS}_o(\mathbf{X})$ and $\mathrm{LOS}_p(\mathbf{X}, P_M)$ denote the InSAR measurements and the predicted displacements in the LOS direction at all ground points $\mathbf{X} = [(x_1,\ y_1),\ (x_2,\ y_2),\ (x_3,\ y_3)\ldots]$.

In reality, it is almost impossible to retrieve P_M using the traditional least squares method due to the high nonlinearity of (7). Yang *et al.* [2] adopted the genetic algorithm (GA) to solve this nonlinear optimization problem. However, the GA converges very slowly or even cannot converge, especially when the number of unknown parameters is large. Hence, a new method named as CA-rPSO has been proposed to solve (8).

1) Cultural Algorithm (CA): The CA was presented by Jin and Reynolds [28] with the key idea of acquiring problem-solving knowledge from the evolution of culture and, in return, applying this knowledge to facilitate optimization. With the advantage of two levels of evolution, i.e., the population and the belief space, the CA has the ability to provide an explicit mechanism for representing, storing, and integrating an individual's and a group's problem-solving behavior and experience [28].

2) Particle Swarm Optimization (PSO): In the population space of the CA, PSO was selected to search the value and location of the optimization particle. PSO was developed by Kennedy and Eberhart [29] based on the stochastic optimization of population social behavior, such as fish schooling or bird flocking. PSO first initializes a group of random particles (i.e., solutions). Then, the best value and location of the particles will be updated once the local peak representing self-experience and the global peak representing social experience have been achieved at each iteration. Without complicated evolution operators (e.g., coding, decoding, crossover and mutation), PSO can obtain the best solutions faster than the GA. In addition, PSO works well for different applications by adjusting only a few parameters.

3) Random PSO (rPSO): Sometimes, PSO easily falls into a local optimum if the particle deviates greatly from the global optimum in early iterations. Thus, a random disturbance operator was introduced into PSO (referred as rPSO) to accelerate the particles' ability to escape local optimums. In addition, velocity was discarded in rPSO to further improve the convergence rate and precision in evolutionary computation.
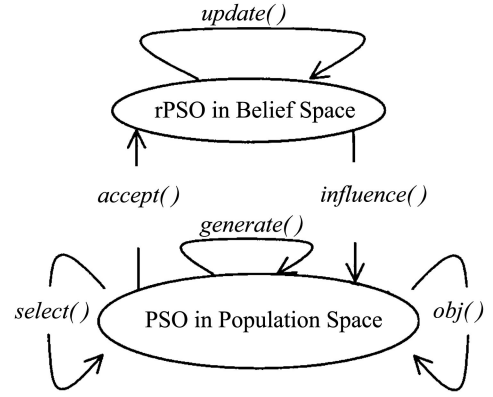

Fig. 3. Framework of CA-rPSO (modified from [28]).

4) CA-rPSO: The framework of CA-rPSO is depicted in Fig. 3. New particles are generated using the *generate()* operator. The *accept()* operator is used to produce beliefs by gleaning the behaviors and experience of selected individuals using PSO in the population space. Then, these beliefs can be used to search the global optimization using rPSO in the belief space, which can also be improved using the *update()* operator. In return, the *influence()* operator can take advantage of this problem-solving knowledge to guide the evolution component of PSO. The performance score of each candidate particle is evaluated by the *obj()* operator. Those that will be the parent particles in the next generation are selected using the *select()* operator.

CA-rPSO, similar to the GA, introduces many stochastic operations to increase the possibility of searching global optimization solutions, which may result in large and random errors in the solutions. Thus, the same measures presented in [2] to eliminate gross error were adopted in this article. First, m CA-rPSO-derived solutions and the corresponding fitness from (8b) are obtained by repeating the CA-rPSO m times. Then, the root mean square error (RMSE) of each parameter in P_M is calculated, and solutions with more than twice the RMSE are eliminated. Finally, assuming that n solutions (denoted by $[P_M^1,\ P_M^2,\ P_M^3,\ \ldots, P_M^n]$) remain, the final parameters $\hat{P}_M$ are calculated by weighting the remaining solutions with their corresponding fitness (denoted by $[\mathrm{fit}(P_M^1),\ \mathrm{fit}(P_M^2),\ \mathrm{fit}(P_M^3),\ \ldots, \mathrm{fit}(P_M^n)]$), which can be expressed as follows:

$$\hat{P}_M = \frac{\sum_1^n \left(\frac{P_M^i}{\mathrm{fit}\left(P_M^i\right)}\right)}{\sum_1^n \left(\frac{1}{\mathrm{fit}\left(P_M^i\right)}\right)}. \tag{9}$$

III. Experiment Using Synthetic Data

A. Synthetic Deformation in the LOS Direction

We suppose that there exist four working panels (i.e., wp1, wp2, wp3, and wp4), whose geometric parameters P_G are shown in Table I. As all the working panels are located in the same seam, we assume for simplicity that the geometric parameters are equal, i.e., $P_{G,1} = P_{G,2} = P_{G,3} = P_{G,4} = P_G$.

TABLE I
GEOMETRIC PARAMETERS OF FOUR WORKING PANELS

ID	Length/m	Width/m	Thickness/m	Dip Angle	Mean Depth/m
wp1	800	300	1.7	3.8	740
wp2	800	400	1.8	2.9	760
wp3	700	360	1.5	3.2	750
wp4	900	320	1.7	3.6	730

TABLE II
ASSUMED PIM PARAMETERS

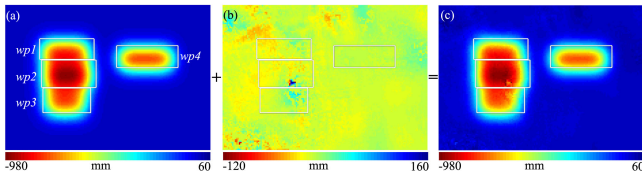| q	$\tan\beta$	θ	b	s_1/H	s_2/H	s_3/H	s_4/H
0.75	2.35	85	0.21	0.1	-0.05	0.11	(0.11, 0.10, 0.09, 0.08, 0.07, 0.06, 0.05)

Fig. 4.   LOS deformation (a) without and (c) with noise; (b) denotes the noise derived from real interferogram.

Consequently, the model parameters can also be considered equal, i.e., $P_{M,1} = P_{M,2} = P_{M,3} = P_{M,4} = P_M$, and all parameters in P_M are shown in Table II. To compare our model with that presented by Yang *et al.* and analyze the influence of s_3 and s_4 on the estimation of P_M, we simulated seven groups of PIM parameters with s_4/H varying from 0.11 to 0.05 while others in P_M are constant. The difference between s_3/H and s_4/H was marked as Δs, i.e., $\Delta s = (s_3 - s_4)/H$.

Next, the 3-D displacements can be generated using the PIM model. The noise-free LOS deformation was calculated by projecting these 3-D displacements into the LOS direction according to the geometric parameters of the SAR sensors, e.g., $\theta = 38.74°$, $\alpha_h = 349.82°$ for ALOS PALSAR, and the result is shown in Fig. 4(a). For simplicity, only one deformation (derived from $s_4/H = 0.05$) is shown in Fig. 4. Subsequently, the noise-free LOS deformation was deteriorated by additional noise [see Fig. 4(b)], which derives from an area without deformation in the real InSAR pair, and the result is shown in Fig. 4(c).

B. Estimation of P_M

We retrieved P_M of the given working panels by applying CA-rPSO to solve (8). A total of 32 particles, 8 particles belonging to the belief space and 24 particles belonging to the population space, were adopted in CA-rPSO in this article. Then, 100 solutions and fitness were obtained by repeating CA-rPSO 100 times. For all seven groups, more than 80 solutions remained after deleting the solutions that had a large bias of greater than twice the RMSE. The eventual P_M (shown in Table III) were attained by weighting the surviving solutions according to (9). In addition, we also retrieved P_M using the model presented by

Yang *et al.* [2] assuming that s_3 and s_4 are equal. These results are also shown in Table III.

C. Accuracy Evaluation

1) Estimation of Model Parameters: We calculated the relative error δ_P of the parameters between the estimation and assumption using (10a), and we show the results in Fig. 5(a) and (b). In addition, we used (10b) to calculate the ratio (ζ_P) of the relative error derived from our model to that from Yang's model for further statistical analysis. The results are shown in Fig. 5(c)

$$\delta_p = \left| \frac{P_M - \hat{P}_M}{P_M} \right| \times 100\% \tag{10a}$$

$$\zeta_p = \left| \frac{P_M - \hat{P}_{M,\,\mathrm{Our}}}{P_M - \hat{P}_{M,\,\mathrm{Yang}}} \right| \tag{10b}$$

where P_M denotes the assumed estimated model parameters. $\hat{P}_M$ denotes the estimated model parameters, while $\hat{P}_{M,\,\mathrm{Our}}$ is derived from our model and $\hat{P}_{M,\,\mathrm{Yang}}$ from Yang's model.

It can be seen from Table III and Fig. 5(a) that the estimation of q, $\tan\beta$, θ_0, and s_3 are in accordance with the assumptions. The relative errors of s_4 and b increase slightly as the difference between s_3 and s_4 increases. The maximum relative errors were no more than 20%. Large errors appeared in the estimation of s_1 (up to 37%) and s_2 (up to 67%), which mainly influence the extent and magnitude of subsidence along the dip direction, i.e., the north-south direction in this experiment. This suggests that the accuracy of parameter retrieval is poorer than others owing to the polar orbit of the satellites, even if we adopt the proposed method.

It can also be seen from Table III and Fig. 5(b) that both our model and Yang's had the same performance in terms of estimation of q, $\tan\beta$, θ_0, s_1, and s_2. However, Yang's model performed poorly at estimating s_3, s_4, and b, whose relative error increased significantly as Δs increased. The relative error of s_3, s_4, and b increased from 1% to 25%, 65%, and 45%, respectively.

It can be seen from Fig. 5(c) that Yang's model performed better at estimating s_3, s_4, and b when $\Delta s = 0$ (i.e., s_3 and s_4 are equal). This means that more model parameters may lead to lower estimation precision, which is the inherent defect of optimization algorithms. However, the maximum relative error derived from our model was no more than 10% (i.e., in b) and is acceptable. In addition, our model performed better when s_3 and s_4 were not equal, even when the difference Δs was very small (e.g., 0.02).

2) Prediction of 3-D Displacement: We retrieved the 3-D displacement fields based on the retrieved parameters for further analysis. The results are shown in Fig. 6(a)–(c). The differences between the retrieved and synthetic 3-D displacement fields were also calculated. Then, we statistically calculated the distribution and RMSE of these differences to quantitatively evaluate the retrieved 3-D displacement fields. We only selected ground points with subsidence larger than 10 mm to avoid the influence of stable points (i.e., outside of the subsidence basin) on the statistical results. The results are shown in Fig. 6(d)–(f). The

TABLE III
ASSUMED PIM PARAMETERS

| Δs	Model	q	$\tan \beta$	θ	b	s_1/H	s_2/H	s_3/H	s_4/H
0.00	Our	0.755	2.348	86.9	0.193	0.065	-0.016	0.106	0.115
	Yang's	0.758	2.332	87.1	0.207	0.065	-0.015	0.111	0.111
0.01	Our	0.751	2.354	86.9	0.189	0.065	-0.018	0.105	0.107
	Yang's	0.755	2.345	86.9	0.192	0.066	-0.018	0.106	0.106
0.02	Our	0.752	2.355	86.8	0.189	0.066	-0.019	0.105	0.097
	Yang's	0.754	2.353	86.8	0.177	0.066	-0.019	0.102	0.102
0.03	Our	0.750	2.357	86.7	0.19	0.067	-0.021	0.105	0.086
	Yang's	0.752	2.364	86.7	0.161	0.065	-0.019	0.097	0.097
0.04	Our	0.749	2.358	86.9	0.185	0.064	-0.019	0.104	0.078
	Yang's	0.748	2.377	86.6	0.146	0.064	-0.020	0.092	0.092
0.05	Our	0.748	2.362	86.7	0.184	0.066	-0.021	0.103	0.069
	Yang's	0.746	2.388	86.7	0.131	0.061	-0.018	0.088	0.088
0.06	Our	0.750	2.359	86.7	0.183	0.066	-0.020	0.103	0.059
	Yang's	0.746	2.397	86.7	0.115	0.061	-0.018	0.083	0.083
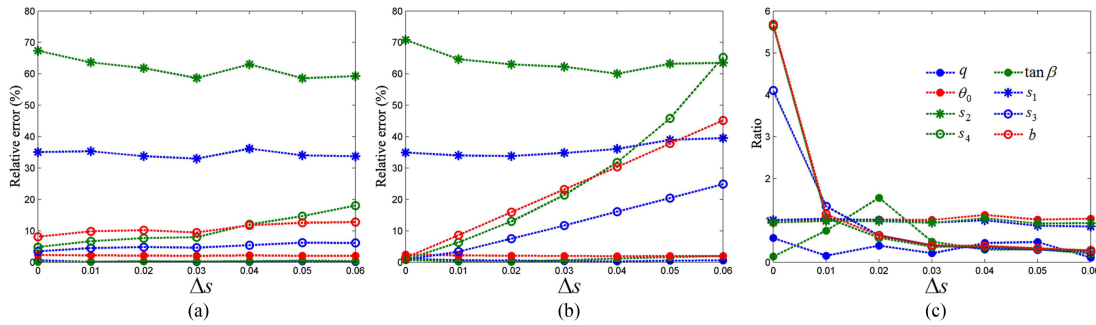
Fig. 5. Relative error derived from (a) our and (b) Yang's model, and the ratio of these errors is shown in (c).
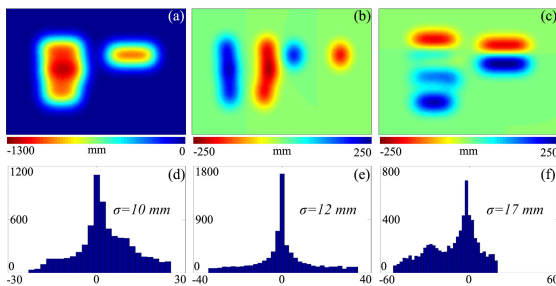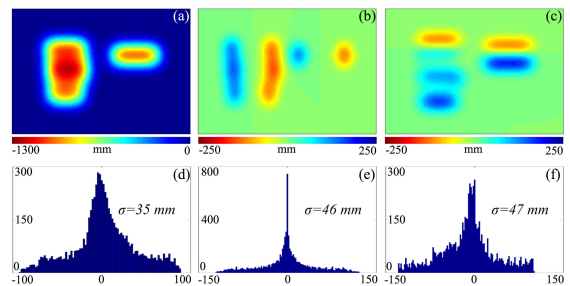

Fig. 6. Retrieved 3-D displacement in the (a) vertical, (b) east-west, and (c) north-south directions using the proposed model, where (d), (e), and (f) are the corresponding histograms of the difference with corresponding synthetic data.

Fig. 7. Retrieved 3-D displacement in the (a) vertical, (b) east-west, and (c) north-south directions using the model presented by Yang *et al.* [2], where (d), (e), and (f) are the corresponding histograms of the differences.

RMSE values are 6.8 and 9.4 mm for the difference in the vertical and east-west directions, respectively. This demonstrates that the proposed method can accurately predict mining-induced 2-D displacement fields.

Since the InSAR measurement is not sensitive to north-south displacement, a small error in the LOS deformation can significantly affect the estimated parameters, especially s_1 and s_2 in this experiment. As seen in Fig. 6(f), the RMSE of the difference in the north-south direction is up to 17 mm. However, the RMSE of the difference amounts only to 7% of the maximal displacement (approximately 250 mm), which meets the requirements of practical applications.

We also retrieved the 3-D displacement fields using the parameters derived from Yang's model [2] and calculated the RMSE of the difference between the retrieved and synthetic data. The results are shown in Fig. 7. The RMSE was up to 35 mm in the vertical direction, 46 mm in the east-west direction, and 47 mm in the north-south direction. Taken together, the proposed method is more accurate than Yang's at retrieving the parameters of the PIM for retrieving or predicting 3-D displacements.
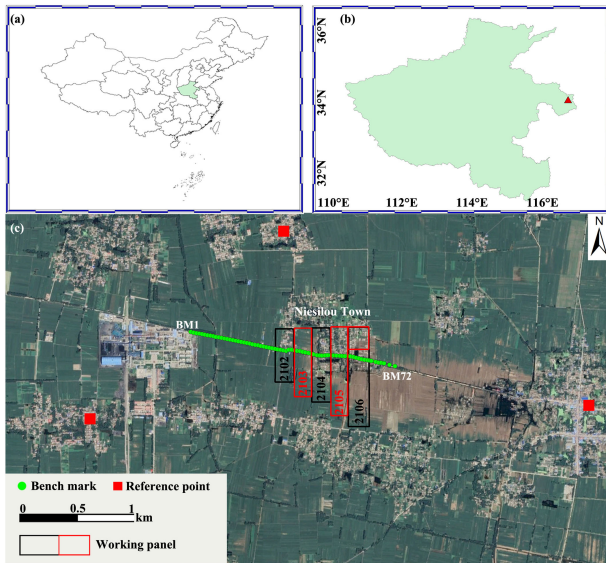
Fig. 8. (a) and (b) Location of the study site in the Xuehu coalfield, Henan Province, China. (c) Three black frames are working panels 2102, 2014, and 2106 superimposed on Google Earth. The black rectangles denote the part of the working panels that were mined during January 2009 and February 2011, while the red rectangles have not been mined.

IV. EXPERIMENT USING REAL DATA

A. Geological Setting

The study site, the Xuehu coalfield, is located in the eastern part of Henan Province, China (see Fig. 8) and has relatively flat topography with an elevation of 38 m above sea level. Most of the coal seams in the Xuehu coalfield are within Carboniferous and Permian sediments. Within this area, there are three working panels (referred as 2102, 2014, and 2016) leading to subsidence derived from DInSAR from January 2009 to February 2011. In addition, two working panels (i.e., 2103 and 2015) will be extracted according to the mine plan. All five working panels are superimposed on a Google Earth Map, which can be seen in Fig. 8.

B. SAR Data and DInSAR Processing Results

We suppose that there exist four working panels (i.e., wp1, wp2, wp3, and wp4), whose geometric parameters P_G are shown in Table I. As all the working panels are located in the same seam, we assume for simplicity that the geometric parameters are equal, i.e., $P_{G,1} = P_{G,2} = P_{G,3} = P_{G,4} = P_G$.

Three ALOS PALSAR acquisitions from an ascending orbit (path 450, frame 670), acquired from January 2009 to February 2011, were used to extract the LOS deformation due to underground mining (see Table IV). The two interferometric pairs whose parameters are summarized in Table V were generated with these PALSAR images acquired in fine beam single polarization. Then, the conventional two-pass DInSAR procedure was used to process the interferometric pairs to derive mining-induced deformation. The topographic phase component is compensated using the TanDEM-X DEM with a pixel spacing of three arc seconds [30], [31]. The atmospheric artifacts in the two interferometric pairs are assumed to be insignificant as the

TABLE IV
PARAMETERS OF WORKING PANELS

Working panel	Date	Strike length	Dip length	Mean thickness	Dip angle	Mean depth
2102	2009.1 –2010.4	166	467	2.72	12	722
2104	2009.11 –2010.9	167	649	2.69	7	748
2106	2010.5 –2011.4	185	871	2.55	4	773
2103	Not yet	147	600	2.70	9	730
2105	Not yet	145	754	2.62	5	760

TABLE V
PARAMETERS OF INTERFEROMETRIC PAIRS

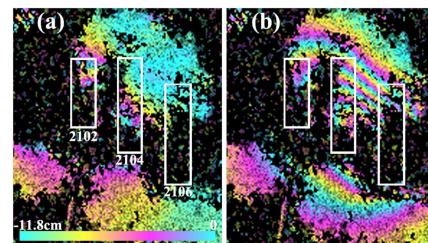| No	Master Date	Slave Data	Spatial Baselines/m
1	20090127	20100130	2192
2	20100130	20110202	1717

Fig. 9. Rewrapped deformation along LOS direction (one color cycle corresponds to 11.8 cm) derived from two interferometric pairs. (a) January 27, 2009 and January 30, 2010. (b) January 30, 2010 and February 2, 2011.

spatial extent of the mine deformation is usually hundreds of meters [1]. The linear-trend phase is considered to be the result of orbital inaccuracies and is eliminated using a bilinear equation. A multilook of 3×1 (azimuth $\times$ slant range) is applied to the interferometric pairs to reduce the phase noise and improve the coherence [32]. In addition, the phase noise is further minimized by applying the Goldstein adaptive filter with the parameter α equal to 0.6 [33]. The interferometric phase is unwrapped using the Delaunay Minimum Cost Flow method [34]. Only those pixels with coherence values above 0.3 in both interferometric pairs are considered for phase unwrapping.

DInSAR is a measure that is relative to reference points. Hence, the selection of an appropriate reference point with known deformation information is crucial to derive reliable results. Preliminary information about deformation and the evaluation of mining excavation in the study area were obtained from leveling measurements. Combining this preliminary information, three points instead of one located in areas unaffected by relevant deformation are selected as reference points highlighted in Fig. 8. In this way, it is possible to minimize the error in DInSAR-derived deformation due to a single misplaced reference point [35]. Finally, the DInSAR-derived deformation is geocoded and transformed into the World Geodetic System 1984 (WGS84) reference system. For the purpose of clearer display, we rewrap the deformation (i.e., one color cycle corresponding to 11.8 cm in the LOS direction) and show the result in Fig. 9. The geocoded deformation will be used to estimate the PIM
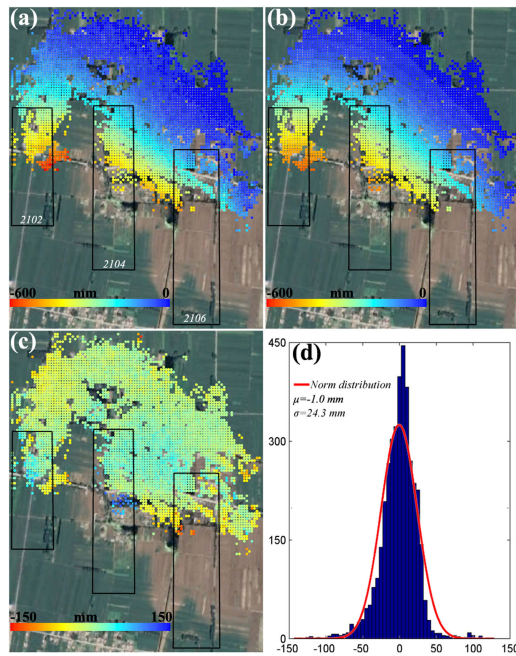
Fig. 10. LOS deformation (a) derived from DInSAR and (b) retrieved by the PIM model between January 27, 2009 and February 2, 2011, superposed on Google Earth. (c) Difference in LOS deformation between DInSAR-derived and PIM-model-retrieved and (d) the corresponding histograms of the difference.

TABLE VI
PARAMETERS OF INTERFEROMETRIC PAIRS

Parameters	q	$\tan\beta$	θ	b	s_1/H	s_2/H	s_3/H	s_4/H
Weighted mean	0.85	1.45	88.5	0.30	0.05	-0.01	0.02	0.04
RMSE	0.05	0.03	1.1	0.03	0.02	0.05	0.02	0.02

parameters, with which we can retrieve and predict the 3-D displacement fields due to underground mining. Then, we will test the reliability of the proposed approach by comparing the retrieved 3-D displacement with leveling data.

C. Estimation of Model Parameters

The mining dates (illustrated in Table IV) of these working panels are different. Thus, the LOS deformation of two periods (from January 27, 2009 to January 30, 2010, from January 30, 2010 to February 2, 2011) was summed to generate the accumulated LOS deformation between January 27, 2009 and February 2, 2011 [shown in Fig. 10(a)].

According to the given geological parameters (i.e., P_G), the accumulated LOS deformation is used to retrieve the model parameters (i.e., P_M) by solving (8) with the CA-rPSO algorithm. It is worth noting that all working panels have the same model parameters as they are located at the same seam with slight differences in depth. First, we attain 100 solutions and corresponding fitness of the P_M by repeating CA-rPSO processing 100 times, with 24 particles in the population space and 8 particles in the belief space. Subsequently, the solutions with gross error greater than twice the RMSE are deleted, after which 81 solutions and fitness remained. Third, the eventual parameters (shown in Table VI) are attained by weighting the
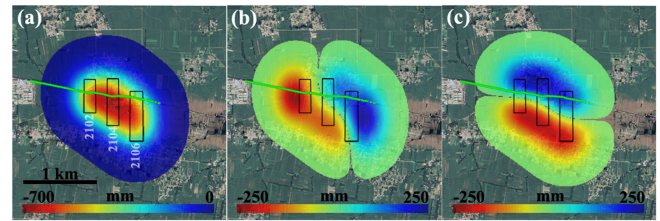

Fig. 11. Retrieved 3-D displacements in the (a) vertical, (b) east-west direction, and (c) north-south directions, superimposed on Google Earth.

surviving solutions with their corresponding fitness [illustrated by (9)].

D. Evaluation of Accuracy

1) Accuracy of Fitting: Having obtained the model parameters of PIM, we retrieve the 3-D displacement fields (shown in Fig. 11) with (2), and then project them to the LOS direction [shown in Fig. 10(b)] with (1). The differences and statistics between the retrieved and DInSAR-derived deformations are shown in Fig. 10(c) and (d). It can be seen that most of the differences vary from –100 to 100 mm. In addition, the differences approximately follow a Gaussian distribution with a mean of –1 mm and a standard deviation of 24 mm (the red line shown in Fig. 10). Statistical analysis demonstrates that the retrieved LOS deformation agrees well with DInSAR-derived deformation.

However, there are approximately 22 points (corresponding to an area of 2200 m^2) where the absolute differences are larger than 100 mm. The maximum difference is up to 140 mm. The main reasons for these large differences are as follows.

1) These differences may be introduced by DInSAR measurement noise, which is likely due to the limited sensitivity of the SAR sensor and possibly has added contributions from atmospheric and/or orbit errors.
2) The differences also may be due to phase unwrapping errors induced by coherence loss in the center (shown in Fig. 9) and the compromising coherence threshold (0.3 is chosen), in addition to large mining-induced deformation, which may exceed the measuring capability of DInSAR.
3) The effects of multiworking panels and abandoned panels may degrade the accuracy of the estimation of PIM parameters [36].
4) The deviation between ground movement due to underground mining and PIM can lead to these differences, especially for points located on the border of the subsidence basin [19] or when geological and mining conditions change.

Nevertheless, the accuracy is acceptable considering that the maximum deformation is up to 670 mm in the study area. Statistical analysis demonstrates that ground movements due to underground mining can be described approximately by the PIM, and the parameters can be reliably estimated by applying the CA-rPSO algorithm to solve (8).

2) Comparison of Vertical Subsidence With in situ *Measurements:* Fig. 12 shows the comparison of vertical subsidence between *in situ* measurements and the results from the improved algorithm. It can be seen that the two measurements correlate
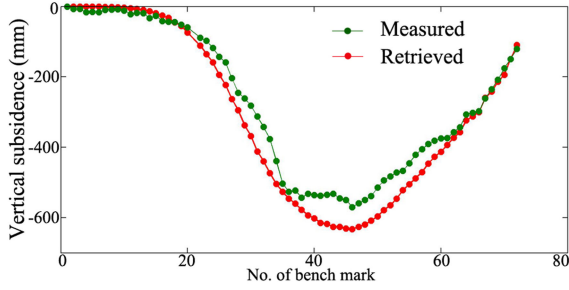
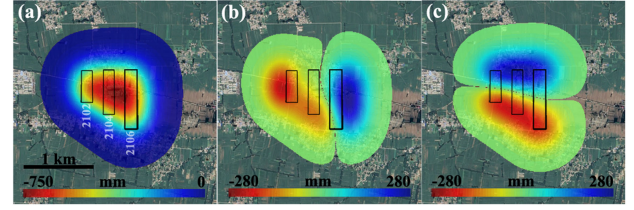Fig. 12. Comparisons of vertical subsidence between the retrieved and the field surveyed measurements.

Fig. 13. Predicted 3-D displacements in the (a) vertical, (b) east-west direction, and (c) north-south directions, superimposed on Google Earth.
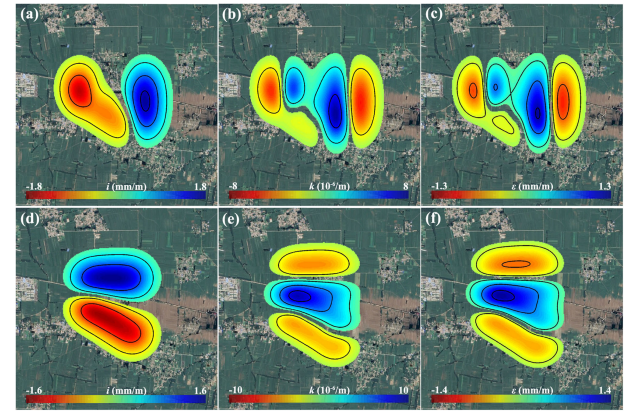

Fig. 14. Predicted (a) and (d) slope i, (b) and (d) curvatures k, (c) and (f) horizontal strains ε in the east-west and north-south directions induced by the excavation of working panels 2102, 2104, and 2106.
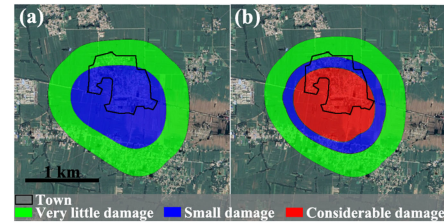

Fig. 15. Assessed damage to buildings after excavation of (a) 2102, 2104, and 2106, and (b) all five working panels.

well with each other. However, vertical subsidence was overestimated at the center of the subsidence basin. There are 24 points in areas where the absolute differences are larger than 60 mm. The maximum difference is up to 99 mm. The reasons for the difference are as follows: in addition to those mentioned earlier, it is also worth noting that there is a difference between the dates of the SAR acquisitions and the ground survey. The mining-induced subsidence rate is highly nonlinear in time. Thus, a slight difference in dates may result in a slightly larger difference in subsidence. In addition, uncertainties in geolocation of the SAR images, changes in geological and mining conditions, and mismatches in targets between the two measurements may also cause this difference.

However, the average absolute difference and the standard deviation between the two measurements is –34 and 37 mm, respectively. The standard deviation amounts only to 5.5% of the maximal subsidence (approximately 670 mm), which meets the requirements for practical applications [21], [37].

3) Comparison of Horizontal Displacement With in situ *Measurements:* The accuracy of the retrieved horizontal displacements cannot be evaluated owing to a lack of *in situ* measurements. However, the previous statistical analysis suggests that the improved algorithm is capable of retrieving vertical subsidence caused by underground mining. Given that the good fitness of the LOS deformation and mining-induce horizontal displacement is generally proportional to the gradient of the vertical subsidence [19], [38], and [39], we infer that the accuracy of the retrieved horizontal displacement should be acceptable in this study area.

Overall, these qualitative and quantitative analyses demonstrate that the improved algorithm is capable of retrieving 3-D displacements due to underground mining.

V. DISCUSSION

A. Damage Evaluation of Buildings After Excavation of Working Panels 2102, 2104, and 2106

Based on the retrieved parameters, the total 3-D displacements produced by the excavation of working panels 2102, 2104, and 2106 can be predicted with the PIM model. The predicted 3-D displacement fields are shown in Fig. 13. It can be seen that the subsiding zone and the horizontal displacement zones match pretty well with the working panels. Mining of the three working panels will result in maximal vertical subsidence of approximately 748 mm just above working panels 2104 and 2106 as

shown in Fig. 13(a)]. The horizontal displacement ranges from –272 to 230 mm in the east-west direction. The peaks appear to the left of working panel 2102 and to the right of 2106 [shown in Fig. 13(b)], respectively. The horizontal displacement ranges from –257 to 217 mm in the north-south direction. The peaks appear in the upward and downward directions of these three working panels [shown in Fig. 13(c)], respectively.

As shown in Fig. 7, the town of Niesilou is located above these working panels. It is necessary to evaluate the damage to buildings. As the safety of a building is more sensitive to slope i, curvature k, and horizontal strain ε, we calculate them using the formulas illustrated in [19] using the predicted 3-D displacement fields. The results are shown in Fig. 14(a)–(f). i, k, and ε range from –1.72 to 1.55 mm/m, from –7.8 to 5.6 10^{-6}/m, and from –1.24 to 0.88 mm/m in the east-west direction, while they range from –1.48 1.60 mm/m, from –9.2 to 4.6 10^{-6}/m, and from –0.74 to 1.36 mm/m in the north-south direction, respectively.

Then, we can assess potential harm to buildings based on the combination of i, k, and ε in both the east-west and north-south directions. The results are shown in Fig. 15(a). To estimate the
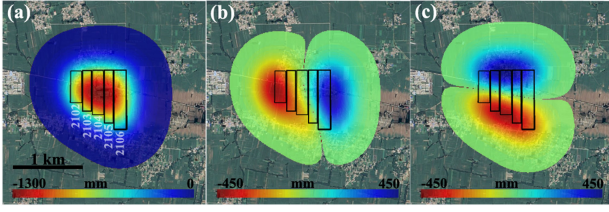
Fig. 16. Predicted 3-D displacements in the (a) vertical, (b) east-west, and (c) north-south directions after excavation of all five working panels, superimposed on Google Earth.
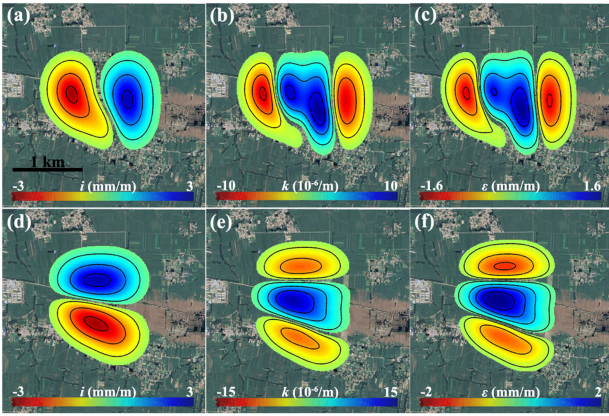

Fig. 17. Predicted (a) and (d) slope i, (b) and (d) curvatures k, (c) and (f) horizontal strains ε in the east-west and north-south directions produced by the excavation of all five working panels (i.e., 2102, 2103, 2104, 2105, and 2106).

percentage of damaged buildings, a grid with a spatial resolution of 100 m × 100 m is first created. Then, the number of grids located on different damage gradations is counted. After that the percentage can be estimated. It can be observed that most of the buildings in the town (approximately 80%) will suffer a small amount of damage. This means that these buildings will still be safe enough to live in after a few necessary repairs based on practical experience and the results of [37].

B. Assessing Potential Damage to Buildings After Excavation of All Five Working Panels

The predicted 3-D displacement fields produced by the excavation of all five working panels are shown in Fig. 16. The subsiding zone and the horizontal displacement zones match pretty well with the working panels. The mining of these five working panels will result in a maximal vertical subsidence of approximately 1300 mm [just above working panels 2104 and 2105 as shown in Fig. 16(a)]. The horizontal displacements range from –420 to 410 mm [see Fig. 16(b)] and from –445 to 400 mm [see Fig. 16(c)] in the east-west and north-south directions, respectively. The locations of the peaks are similar to previous results shown in Fig. 13.

Again, we calculate the slope i, curvature k, and horizontal strain ε and show them in Fig. 17(a)–(f). i, k, and ε range from –2.68 to 2.73 mm/m, from –10 to 8.5 10^{-6}/m, and from –1.60 to 1.27 mm/m in the east-west direction, while they range from –2.75 to 2.80 mm/m, from –14 to 8.2 10^{-6}/m, and from –1.29 to

2.10 mm/m in the north-south direction, respectively. Then, we assess once again the potential damage to buildings based on the combination of i, k, and ε in both the east-west and north-south directions. As shown in Fig. 15(b), we find that almost all of the buildings in the town (approximately 80%) will suffer damage, and approximately 75% will suffer considerable damage. In light of this, special attention should be paid and special mining methods should be adopted by the mining industry and local government to deal with this issue, such as the following:

1) relocating the town;
2) adopting the backfill mining method to reduce ground deformation;
3) adopting a larger size of protective coal pillars as needed.

VI. CONCLUSION

This article presented an improved algorithm for retrieving 3-D displacements induced by underground mining based on the LOS deformation derived from DInSAR. Without any simplification, all parameters of the PIM model are involved in the improved algorithm. To retrieve the model parameters, we presented a new method, i.e., CA-rPSO. In addition, considering the fact that multiple working panels are mined successively, the interaction between multiple working panels was considered in the improved algorithm.

We first carried out a simulated experiment to validate the accuracy of the presented algorithm. The RMSEs from comparing the simulated and the retrieved 3-D displacements were 10, 12, and 17 mm in the vertical, east-west, and north-south directions, respectively. It is worth noting that the accuracy of the retrieved 3-D displacements is different in different directions.

Afterward, the presented algorithm was used to retrieve the parameters of the PIM model over Xuehu mining area in China based on the accumulated LOS deformation derived from three ALOS PALSAR acquisitions. Then, the 3-D displacement components were retrieved based on the PIM model. These displacement fields coincide spatially with the evolution of mining excavation. The retrieved vertical displacements were successfully compared with field surveys, with an RMSE of 37 mm. Besides, based on the PIM model and the retrieved model parameters, we predicted the final 3-D displacements when all working panels have been extracted. These displacement fields coincided spatially with the location of the working panels. Assessing potential building damage based on the predicted displacements, we find that most of the buildings in the town (approximately 75%) will suffer considerable damage. The method described in this study has been proven to be an encouraging technique for retrieving and predicting the 3-D displacement caused by underground mining and assessing the potential harm to buildings.

APPENDIX A

CALCULATION OF SLOPE (I), CURVATURE (K) AND HORIZONTAL STRAIN (ε)

Once the 3-D displacements have been predicted (shown in Figs. 13 and 16), the slope (i), the curvature (k), and the

horizontal strain (ε) at a ground point (e, n) can be calculated by [19]

$$\begin{cases} i_E(e,n) = \frac{1}{\Delta l_E}\left[D_V(e+1,n) - D_V(e,n)\right] \\ i_N(e,n) = \frac{1}{\Delta l_N}\left[D_V(e,n+1) - D_V(e,n)\right] \end{cases} \quad \text{(A1)}$$

$$\begin{cases} k_E(e,n) = \frac{1}{\Delta l_E}\left[i_E(e+1,n) - i_E(e,n)\right] \\ k_N(e,n) = \frac{1}{\Delta l_N}\left[i_N(e,n+1) - i_N(e,n)\right] \end{cases} \quad \text{(A2)}$$

$$\begin{cases} \varepsilon_E(e,n) = \frac{1}{\Delta l_E}\left[D_E(e+1,n) - D_E(e,n)\right] \\ \varepsilon_N(e,n) = \frac{1}{\Delta l_N}\left[D_N(e,n+1) - D_N(e,n)\right] \end{cases} \quad \text{(A3)}$$

where the subscripts E and N denote the east-west and north-south directions. Δl denotes the distance between adjacent ground points. The results are shown in Figs. 14 and 17.

APPENDIX B

ASSESSMENT OF MINING-INDUCED BUILDING DAMAGE

In China, the gradation of building damage (shown in Table VII) is determined based on the characteristics of ground deformation, i.e., i, k, and ε.

TABLE VII
GRADATION OF DAMAGE OF BUILDINGS

G	i(mm/m)	k (10^{-6}/m)	ε(mm/m)	Possible degree of damage
I	≤ 2	≤ 3	≤ 0.2	Very little
II	≤ 4	≤ 6	≤ 0.4	Small
III	≤ 6	≤ 10	≤ 0.6	Considerable
IV	> 6	> 10	> 0.6	Serious

The area (A) of building damage can then be calculated by

$$A = A(i) \cup A(k) \cup A(\varepsilon) \quad \text{(B1)}$$

where operator $\cup$ denotes the union. $A(i)$, $A(k)$, and $A(\varepsilon)$ denote the area of building damage based on $G(i)$, $G(k)$, and $G(\varepsilon)$, respectively. $G(i)$, $G(k)$, and $G(\varepsilon)$ denote the gradation of damage based on the i, k, and ε, respectively. i, k, and ε can be calculated based on (A1)–(A3). The results calculated based on (B1) are shown in Fig. 15.

Note that Table VII was created for buildings of materials commonly applied in the rural of China where the brick houses are mainly detached and have no more than two floors. The characters and the corresponding critical values used for evaluating the damage of buildings are different for different constructions in different countries.

REFERENCES

[1] H. M. Ng, L. Ge, Z. Du, S. Wang, and C. Ma, "Satellite radar interferometry for monitoring subsidence induced by longwall mining activity using Radarsat-2, Sentinel-1 and ALOS-2 data," *Int. J. Appl. Earth Observ. Geoinf.*, vol. 61, pp. 92–103, 2017.

[2] Z. F. Yang, Z. W. Li, J. J. Zhu, J. Hu, Y. J. Wang, and G. L. Chen, "inSAR-based model parameter estimation of probability integral method and its application for predicting mining-induced horizontal and vertical displacements," *IEEE Trans. Geosci. Remote Sens.*, vol. 54, no. 8, pp. 4818–4832, Aug. 2016.

[3] Z. Du, L. Ge, X. Li, and H. M. Ng, "Subsidence monitoring in the Ordos basin using integrated SAR differential and time-series interferometry techniques," *Remote Sens. Lett.*, vol. 7, no. 2, pp. 180–189, 2016.

[4] H. Fan, X. Gao, J. Yang, K. Deng, and Y Yang, "Monitoring mining subsidence using a combination of, phase-stacking and offset-tracking methods," *Remote Sens.*, vol. 7, no. 7, pp. 9166–9183, 2015.

[5] F. Ma, H. Zhao, R. Yuan, and J. Guo, "Ground movement resulting from underground backfill mining in a nickel mine (Gansu Province, China)," *Nature Hazards*, vol. 77, no. 3, pp. 1475–1490, 2015.

[6] K. Xia *et al.*, "In situ monitoring and analysis of the mining-induced deep ground movement in a metal mine," *Int. J. Rock Mechanics Mining Sci.*, vol. 109, pp. 32–51, 2018.

[7] L. Zhang, X. Ding, and Z Lu, "Ground settlement monitoring based on temporarily coherent points between two SAR acquisitions," *ISPRS J. Photogrammetry Remote Sens.*, vol. 66, no. 1, pp. 146–152, 2011.

[8] D. Massonnet *et al.*, "The displacement field of the Landers earthquake mapped by radar interferometry," *Nature*, vol. 364, no. 6433, pp. 138–142, 1993.

[9] H. A. Zebker, P. A. Rosen, R. M. Goldstein, A. Gabriel, and C. L. Werner, "On the derivation of coseismic displacement fields using differential radar interferometry: The Landers earthquake," *J. Geophys. Res. Solid Earth*, vol. 99, no. B10, pp. 19617–19634, 1994.

[10] L. Cascini, D. Peduto, G. Pisciotta, L. Arena, S. Ferlisi and G. Fornaro, "The combination of dinsar and facility damage data for the updating of slow-moving landslide inventory maps at medium scale," *Natural Hazards Earth Syst. Sci.*, vol. 13, no. 6, pp. 1527–1549, 2013.

[11] M. Motagh *et al.*, "Land subsidence in Iran caused by widespread water reservoir overexploitation," *Geophys. Res. Lett.*, vol. 35, 2008, Art. no. L16403.

[12] C. Carnec and C. Delacourt, "Three years of mining subsidence monitored by SAR interferometry, near Gardanne, France," *J. Appl. Geophys.*, vol. 43, no. 1, pp. 43–54, 2000.

[13] T. Strozzi, U. Wegmuller, L. Tosi, G. Bitelli, and V. Spreckels, "Land subsidence monitoring with differential SAR interferometry," *Photogrammetric Eng. Remote Sens.*, vol. 67, no. 11, pp. 1261–1270, 2001.

[14] H. M. Ng, L. Ge, K. Zhang, and X. Li, "Estimating horizontal and vertical movements due to underground mining using ALOS PALSAR," *Eng. Geol.*, vol. 143–144, pp. 18–27, 2012.

[15] L. He, L. Wu, S. Liu, Z. Wang, C. Su, and S. N. Liu, "Mapping two-dimensional deformation field time-series of large slope by coupling DInSAR-SBAS with MAI-SBAS," *Remote Sens.*, vol. 7, no. 9, pp. 12440–12458, 2015.

[16] N. B. D. Bechor and H. A. Zebker, "Measuring two-dimensional movements using a single InSAR pair," *Geophys. Res. Lett.*, vol. 33, no. 16, 2006, Art. no. L16311.

[17] H. S. Jung, J. S. Won, and S. W. Kim, "An improvement of the performance of multiple-aperture SAR interferometry (MAI)," *IEEE Trans. Geosci. Remote Sens.*, vol. 47, no. 8, pp. 2859–2869, Aug. 2009.

[18] Z. Yang *et al.*, "Deriving time-series three-dimensional displacements of mining areas from a single-geometry InSAR dataset," *J. Geodesy*, vol. 92, no. 5, pp. 529–544, 2017.

[19] G. He, L. Yang, and G. Lin, *Mining Subsidence Engineering*, (in Chinese), Xuzhou, China: Press China Univ. Mining Technol., 1994.

[20] Z. W. Li *et al.*, "Retrieving three-dimensional displacement fields of mining areas from a single InSAR pair," *J. Geodesy*, vol. 89, no. 1, pp. 17–32, 2015.

[21] Z. F. Yang *et al.*, "An extension of the inSAR-based probability integral method and its application for predicting 3-D mining-induced displacements under different extraction conditions," *IEEE Trans. Geosci. Remote Sens.*, vol. 55, no. 7, pp. 3835–3845, Jul. 2017.

[22] Y. Fialko, M. Simons, and D. Agnew, "The complete (3-d) surface displacement field in the epicentral area of the 1999 Mw7.1 hector mine earthquake, california, from space geodetic observations," *Geophys. Res. Lett.*, vol. 28, no. 16, pp. 3063–3066, 2001.

[23] H. M. Ng *et al.*, "Deformation mapping in three dimensions for underground mining using InSAR-southern highland coalfield in New South Wales, Australia," *Int. J. Remote Sens.*, vol. 32, no. 20, pp. 7277–7256, 2011.

[24] R. W. Seedsman and G. Watson, "Sensitive infrastructure and horizontal ground movementsat Newstan Colliery," in *Proc. 5th Triennial Conf. Coal Mine Subsidence Current Pract. Issues*, Aug. 2001, pp. 171–179.

[25] J. Litwiniszyn, "Application of the equation of stochastic processes to mechanics of loose bodies," *Archives Mechanics*, vol. 8, no. 4, pp. 393–411, 1956.

[26] B. Liu and G. Liao, *Basic Law of Ground Surface Movement Due to Coal Mining*. Beijing, China: Industrial Press China, 1965.

[27] P. Li, Z. Tan, and L. Yan, "A shaft pillar mining subsidence calculation using both probability integral method and numerical simulation," *Comput. Model. Eng. Sci.*, vol. 117, no. 2, pp. 231–250, 2018.

[28] X. Jin and R. G. Reynolds, "Using knowledge-based evolutionary computation to solve nonlinear constraint optimization problems: A cultural algorithm approach," in *Proc. Congress Evol. Comput.*, Jul. 1999, pp. 1672–1678.

[29] J. Kennedy and R. Eberhart, "Particle swarm optimization," in *Proc. Int. Conf. Neural Netw.*, Nov./Dec. 1995, pp. 1942–1948.

[30] M. Przylucka, H. Gerardo, G. Marek, C. Davide, and B. Marta, "Combination of conventional and advanced DInSAR to monitor very fast mining subsidence with TerraSAR-X data: Bytom City (Poland)," *Remote Sens.*, vol. 7, no. 5, pp. 5300–5328, 2015.

[31] B. Wessel, M. Huber, C. Wohlfart, U. Marschalk, D. Kosmann, and A. Roth, "Accuracy assessment of the global tandem-x digital elevation model with GPS data," *ISPRS J. Photogrammetry Remote Sens.*, vol. 139, pp. 171–182, 2018.

[32] C. Zhu, Y. Zhang, J. Zhang, L. Zhang, S. Long, and H. Wu, "Recent subsidence in Tianjin, China: Observations from multi-looking TerraSAR-X InSAR from 2009 to 2013," *Int. J. Remote Sens.*, vol. 36, no. 23, pp. 5869–5886, 2015.

[33] R. M. Goldstein and C. L. Werner, "Radar interferogram filtering for geophysical applications," *Geophys. Res. Lett.*, vol. 25, no. 21, pp. 4035–4038, 1998.

[34] M. Costantini, "A novel phase unwrapping method based on network programming," *IEEE Trans. Geosci. Remote Sens.*, vol. 36, no. 3, pp. 813–821, May 1998.

[35] S. Fiaschi, D. Closson, A. N. Karaki, P. Pasquali, P. Riccardi, and M. Floris, "The complex karst dynamics of the Lisan Peninsula revealed by 25 years of DInSAR observations. Dead Sea, Jordan," *ISPRS J. Photogrammetry Remote Sens.*, vol. 130, pp. 358–369, 2017.

[36] W. Zhou, H. Zhang, and W. Zhong, "Study of getting surface subsidence parameters under the effect of multi-working-face mining," *J. China Coal Soc.*, vol. 25, no. 3, pp. 260–263, 2000.

[37] State Bureau of Coal Industry, *Regulations of Coal Pillar Design and Extractionfor Buildings, Water Bodies, Railways, Main Shafts and Roadways*. Beijing, China: Coal Industry Press, 2000.

[38] H. Kratzsch, *Mining Subsidence Engineering*. New York, NY, USA: Springer, 1983.

[39] S. S. Peng, *Surface Subsidence Engineering*. Littleton, CO, USA: Soc. Mining, Metallurgy, Exploration, Inc., 1992.

Chuanguang Zhu was born in Chengwu, China, in 1984. He received the B.S. degree in surveying and mapping, and the Ph.D. degree in photogrammetry and remote sensing from China University of Mining and Technology, Xuzhou, China, in 2009 and 2015, respectively.

From February 2012 to May 2015, he was with the Chair for China Academy of Surveying & Mapping (CASM), where he mainly worked on synthetic aperture radar interferometry (InSAR), differential InSAR and multitemporal InSAR. He is currently a Lecturer with the Hunan University of Science & Technology, Xiangtan, China. His current research interests include InSAR data processing.

Zhengshuai Wang received the master's degree in cartography and geographical information engineering, and the Ph.D. degree in geodesy and surveying engineering from the China University of Mining and Technology, Xuzhou, China, in 2005 and 2011, respectively.

He is currently a Lecturer with Jiangsu Normal University, Xuzhou. His current research interests include monitoring mine disaster, modeling and predicting the ground displacement induced by mining.

Peixian Li was born in Juye, China, in 1983. He received the B.S. degree in surveying and mapping, and the Ph.D. degree in geodetic surveying from the China University of Mining and Technology, Xuzhou, China, in 2007 and 2012, respectively.

He is currently an Assistant Professor with the China University of Ming and Technology, Beijing, China. His research interests include mining subsidence prediction and control.

Mahdi Motagh was born in Tehran, Iran, in 1975. He received the B.Sc. degree in surveying engineering and the M.Sc. degree in geodesy from the University of Tehran, Tehran, Iran, in 1998 and 2002, respectively, and the Ph.D. degree in earth sciences from the University of Potsdam, Potsdam, Germany, in 2007.

As of 2007, he was a Postdoctoral Scientist with GFZ German Research Center for Geosciences in Potsdam, Germany, where he became a Permanent Research Staff, in 2011. In 2017, he became a Professor for radar remote sensing with Leibniz University Hanover, Hannover, Germany. He also has a Guest Professorship with Wuhan University, Wuhan, China.

Liya Zhang was born in Zhaoxian, China, in 1982. He received the B.S. degree in surveying and mapping, and the Ph.D. degree in geodesy and surveying engineering from the China University of Mining and Technology, Xuzhou, China, in 2006 and 2012, respectively.

He is currently a Lecturer with the Hunan University of Science & Technology, Xiangtan, China. His current research interests include mining subsidence and backfill mining.

Zongli Jiang received the master's degree in tectonic geology from Central South University, Changsha, China, in 2004, and the Ph.D. degree in cartography and GIS from the State Key Laboratory of Cryospheric Sciences, Cold and Arid Regions Environmental and Engineer Research Institute, Chinese Academy of Sciences, Lanzhou, China in 2011.

He is currently an Associate Professor with the Hunan University of Science & Technology, Xiangtan, China. His research interests include velocity monitoring and stability analyzing of glacier using SAR technology.

Sichun Long received the master's and Ph.D. degrees in geodesy and surveying engineering from Wuhan University, Wuhan, China, in 2005 and 2009, respectively.

From September 2010 to June 2013, he was a Postdoctoral Fellow with the School of Geosciences and Info-Physics, Central South University. In 2015, he became a Professor for the geodesy and surveying engineering with the Hunan University of Science & Technology, Xiangtan, China. He is currently the leader of the Key Laboratory of Coal Resources Clean-utilization & Mine Environment Protection of Hunan Province. His research interests include the InSAR, disaster monitoring and early warning.